Original research article

SHM Structural Health Monitoring

Structural Health Monitoring
1–18

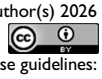

DOI: 10.1177/14759217261446879
journals.sagepub.com/home/shm
Sage

Remote detection of internal and subsurface damage in wind turbine blades using acoustic beamforming and infrared thermography

Yanan Zhang[1], Sumit K. Pal[1], Daniele Ragni[1], Roger M. Groves[1] and Simon J. Watson[1]

Abstract

This work experimentally investigated the feasibility and complementarity of aeroacoustic and infrared thermography (IRT) techniques for detecting damage in rotating wind turbine blades under controlled wind tunnel conditions. Two representative types of damage were considered: trailing edge cracks and internal shear web delamination, created in the scaled blades manufactured in-house. Experiments were conducted in the open jet facility at Delft University of Technology. Acoustic measurements using a two-dimensional microphone array revealed that trailing edge cracks induce distinct tonal noise modifications, which depend on the effective trailing edge thickness and are captured through spectral analysis and acoustic beamforming. The crack-induced tonal noise peaks at a trailing-edge-thickness-based Strouhal number, St_h, between 0.15 and 0.25. IRT, by contrast, are highly sensitive to internal structural features; delaminated regions exhibited localized temperature variations due to changes in thermal properties. Principal component thermography was applied to further enhance the visualization of the internal shear webs and internal delamination. The results demonstrate that the use of aeroacoustic and IRT methods provides a complementary strategy for detecting both edge and internal damage in wind turbine blades.

Keywords

blade damage detection, subsurface and internal damage, acoustic beamforming, infrared thermography, remote measurement

Introduction

Wind energy is an important renewable energy source, with the number of installed wind turbines steadily increasing.[1,2] Wind turbine blades, owing to their operating loads and direct exposure to the environment, are especially vulnerable to damage.[3] This includes surface damage, such as leading edge erosion[4] and coating delamination,[5] and subsurface or internal structural damage, including trailing edge cracks,[6] structural delamination,[7] and fatigue-related failures.[8] Surface damage, which generally leads to observable visual changes on the blade surface, can be effectively identified using, for example, high-resolution cameras[9] without relying on indirect inference or complex signal inversion, whereas identification of subsurface or internal damage remains much more challenging.[9]

The high cost and challenges of maintenance make damage detection and continuous monitoring crucial for ensuring efficiency, reliability, and safety of operation.[10–12] Remote damage detection based on non-contact techniques, including acoustics,[13] infrared thermography (IRT),[14] and laser Doppler vibrometry,[15] enables more flexible and convenient inspections, suitable for use on rotating blades in contrast to conventional human visual inspections[16] which require a turbine stop or methods using contact sensors which require attachment to the blades.[17,18]

Aeroacoustic measurements are used to investigate noise generated by the motion of airflow and its

[1]Faculty of Aerospace Engineering, Delft University of Technology, the Netherlands

Corresponding author:
Yanan Zhang, Faculty of Aerospace Engineering, Delft University of Technology, Kluyverweg 1, Delft 2629HS, the Netherlands
Email: Yanan.Zhang@tudelft.nl

interactions with solid bodies.[19,20] Numerous studies in aeroacoustics have been conducted to reduce noise from wind turbines.[21,22] In recent years, an aeroacoustics-based method[23] has been applied to detect damage in wind turbine blades. When damage occurs on the blade surface or the edge, the resulting changes in geometry and surface roughness can affect the surrounding flow field and boundary layer transition, thereby altering the aerodynamic noise generation. This noise can be captured by microphones placed in the far field, enabling a fully remote and non-contact approach, which has recently been used to detect wind turbine blade damage in wind farms.[24,25]

In the authors' previous studies,[26–28] the detection of blade trailing edge cracks and leading edge erosion was investigated for airfoils under various inflow conditions. The presence of a trailing edge crack effectively thickens the trailing edge, which can increase the boundary layer velocity gradient and the intensity of coherent vortex shedding from the trailing edge, thereby producing a measurable tonal component in the noise spectrum. As the crack size increases, the length scale of the coherent vortex structures decreases, resulting in a shift of the tonal peak toward lower frequencies.[26,28] In the case of leading edge erosion, the modifications to the noise spectra due to damage depend strongly on the inflow condition. Under clean inflow, erosion promotes an earlier boundary layer transition, altering the trailing edge noise properties from laminar-boundary-layer instability noise to turbulence noise. In contrast, under turbulent inflow with a short turbulence length scale in the lab environment, the trailing edge noise alone cannot effectively indicate the presence of erosion. Instead, changes in the leading edge noise spectrum reveal that erosion reduces the mid-to-high frequency components, due to greater distortion of the incoming turbulence caused by the enlarged stagnation region in front of the eroded leading edge.[27] The aeroacoustics-based method is relatively straightforward to implement using microphones for rotating wind turbine blades, owing to the nature of aerodynamic noise generation and propagation[20] and is effective primarily for surface or edge damage (for example, leading edge erosion and trailing edge cracks), as such defects can induce sufficient aeroacoustic variations. However, it is incapable of detecting deep internal structural damage.

IRT has emerged as a valuable tool for non-contact blade damage detection, in particular, allowing the identification of internal and subsurface defects by capturing heat transfer anomalies in environments with temperature differences.[29] Internal or subsurface defects, such as cracks or delamination, introduce air voids that disrupt heat transfer within the composite material, leading to measurable changes in the surface temperature distribution.[29,30] During operation with an external heat source, such as the natural solar heat source, the surface temperature above an internal defect rises faster than that of the surrounding healthy regions, as the defect impedes heat flux and modifies the local thermal diffusion path.[30–32] This localized increase of temperature leads to a detectable thermal anomaly in images captured by infrared cameras, enabling the identification of subsurface or internal damage by analyzing blade surface temperature distributions and gradients.[33] Previous physics-based models grounded in heat transfer theory have been used to predict thermal contrasts caused by subsurface defects and evaluate the defect depth, providing insights into the relationship between material properties, heating conditions, and thermal responses.[14,34] In parallel, data-driven methods, particularly those based on machine learning, have been employed to automatically identify damage patterns and classify damage types from large sets of thermal images.[35,36] On-site inspections have demonstrated the feasibility of using IRT for internal structural damage detection in real wind farm environments.[37,38]

In real-world applications, IRT usually suffers from limited spatial resolution, making the detection of small structural defects, especially near blade edges, challenging.[39] Consequently, higher spatial resolution can only be achieved by restricting the field of view (FOV) of the infrared camera to a relatively small, localized region of the blade surface. However, narrowing the FOV to improve spatial resolution causes the blade to move rapidly across the imaged region, thereby inducing motion blur[40–42] and making the detection of edge damage especially difficult in practice. The motion-induced blurring can be mitigated by employing infrared cameras with a very short integration time, which is an expensive option for practical applications.

Blade damage detection methods using microphones and IRT are promising due to their potentially straightforward implementation in practice.[24,43] However, the limitations of the individual methods discussed above demonstrate that no single technique can provide complete and reliable detection of all types of damage under real operating conditions. In this work, an experimental investigation is conducted to assess the complementarity of aeroacoustics and IRT for the detection of subsurface and internal damage in wind turbine blades.

The main experiment was performed in the open jet facility (OJF) of Delft University of Technology (TU Delft) using a scaled wind turbine. This was supplemented by initial verification measurements on static blades in an acoustic wind tunnel. The study focused on several in-house manufactured blades with two types of internal and subsurface damage, including

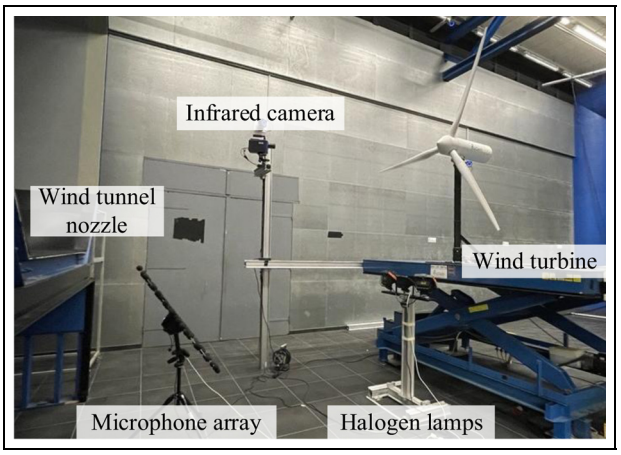

Figure 1. Experimental setup.
Note. The distribution of the microphones on the planar array is shown in Figure 4(a).

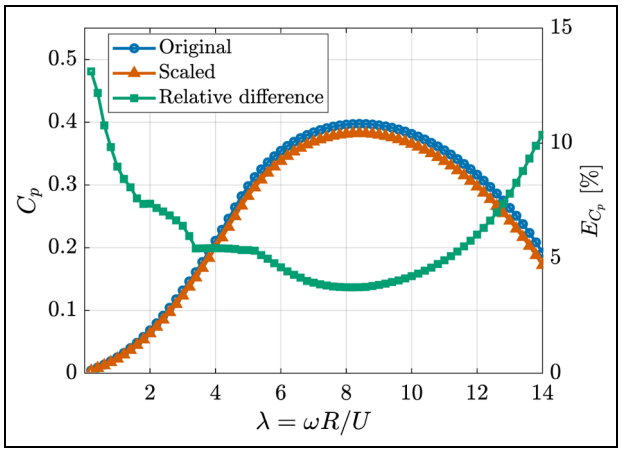

Figure 2. The power coefficients of the original and scaled wind turbines and their difference at various tip speed ratios.

internal shear web delamination and a trailing edge crack. Acoustic data were recorded by a Bionic M-112 microphone array. Acoustic beamforming[44] and source power integration[45] techniques were applied to analyze the noise sources and isolate background noise. Blade surface temperatures were measured using a Cedip Titanium infrared camera, and the thermal images of the damaged blades were compared with those of a healthy (baseline) blade under the same test conditions. Principal component (PC) thermography (PCT)[46] was applied to decompose and reconstruct the thermal data to suppress noise and enhance the visibility of subtle damage-related features.

The remainder of this paper is organized as follows. The second section introduces the methodology, including a detailed description of the experimental setup and the procedures for acoustic and thermal measurements. The third section presents pre-checks and verification tests on non-rotating blades, providing a benchmark for comparison with the rotating results. The fourth section reports the experimental results of the rotating tests and discusses the performance of both the aeroacoustic and IRT approaches. Finally, the fifth section summarizes the main findings of this work and offers an outlook for future research.

Methodology

Wind tunnel facility and wind turbine

The main experiment was performed in the OJF, which has an octagonal nozzle with a size of 2.85 × 2.85 m, as shown in Figure 1. The wind tunnel can reach a maximum wind speed of 34 m/s with a turbulence intensity of 0.5% measured at approximately 1 m from the nozzle. The free-stream area contracts with a 4.75° semi-angle along the length of the jet, due to the development of the jet shear layer. A detailed description and characterization of the flow in the OJF were reported in the study by Lignarolo et al.[47]

The test wind turbine was scaled from a 2.3-MW NM80 wind turbine,[48–50] which has a rotor radius of 40.04 m. The rotor was downscaled to a radius of $R = 1250$ mm (scale factor 1:32). The power captured by the rotor is transmitted to a brushless motor via a gearbox with a gear ratio of 1:5. The motor was controlled by an iPOS8015 four-quadrant controller, enabling the wind turbine to operate at a constant rotational speed. The generated power was fed to the grid through a Chroma 62000D bidirectional DC power supply. The wind turbine was fixed on an adjustable table, making the rotating center approximately aligned with the nozzle center. The distance between the rotor and the nozzle edge was approximately 3.75 m. All three blades were manually changeable, allowing for the testing of different blades and pitch angles. In the experiment, the pitch angle of the blade was fixed at 0°. The aerodynamic performance for both the original and scaled wind turbines was estimated using Blade Element Momentum Theory (BEMT). The curves of the power coefficient, C_p, against the tip speed ratio, $\lambda = \omega R/U$ (where ω and R are the angular rotational speed and radius of the rotor, respectively; and U is the wind speed), are shown in Figure 2. The relative difference between the scaled and original wind turbines, $E_{C_p} = \left|C_{p,\text{scaled}} - C_{p,\text{orignal}}\right| / C_{p,\text{orignal}}$, is also presented for comparison. The scaled wind turbine shows a slightly lower power coefficient at a given tip speed ratio compared to the original model. This is attributed to the lower Reynolds number of the scaled model, which reduces the aerodynamic efficiency of the airfoils with a lower lift-to-drag ratio.[51,52]

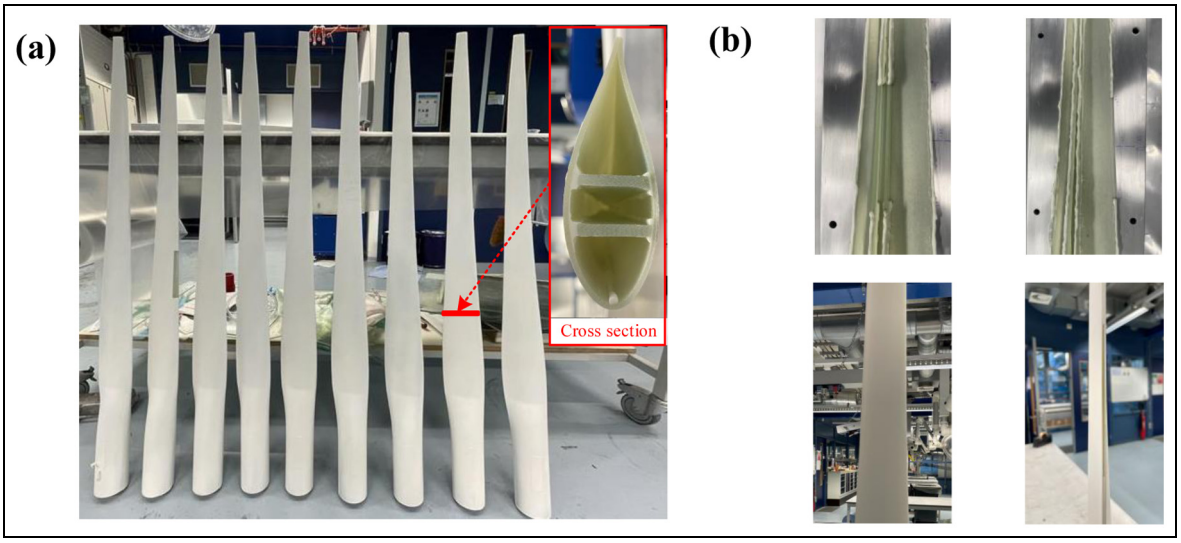

Figure 3. Blade samples: (a) the manufactured blades and (b) the designed artificial damage, top row: raw blades before gluing or painting, showing (from left to right) internal delamination and trailing edge crack; bottom row: the corresponding damage in the finished blades (the internal delamination is invisible).

Blade samples

The blades, shown in Figure 3(a), were manufactured by the authors at the Delft Aerospace Structures and Materials Laboratory (DASML) of TU Delft. The length of the blade, excluding the connector to the wind turbine hub, is $L = 1200$ mm. To balance structural representativeness and manufacturability in the laboratory, the blade geometry was simplified and divided into four parts: the pressure and suction shells and two internal shear webs, as shown in the cross section in the inset to Figure 3(a). The local trailing edge surface of the blade was slightly modified to be flat with a zero solid angle,[53] making it possible to glue additional tape to modify the thickness. Two internal shear webs are located at 26.0% and 42.5% of the local chord length, C, measured from the leading edge, respectively. For each part, an aluminum mold was made, and the raw components were produced using a standard vacuum infusion process for glass-fiber reinforced composites.[54] The laminate consisted of layers cut from a 200 g/m^2 bidirectional glass-fiber fabric (0°/90° plain weave). For the pressure and suction shells, 10 layers were applied, resulting in a cured thickness of approximately 2 mm, while the internal shear webs were composed of 20 layers, yielding a thickness of about 4 mm. Curing was performed using Resoltech 1800 resin with 1803 hardener at room temperature. The blades were painted with white matte spray to ensure a high and uniform surface emissivity and to minimize infrared reflections during thermal measurements. The thermal emissivity was estimated as 0.91 for the white matte blade surface.[55,56] The final manufactured blades are shown in the larger photo in Figure 3(a).

Two blades were designed with artificial damage: internal shear web delamination and trailing edge crack, as shown in Figure 3(b) from left to right. The internal delamination and trailing edge crack were created by intentionally leaving out a section of adhesive during assembly. Both types of damage are located at the mid-span of the blade (50% R) and extend over a length of 125 mm (10% R). A summary of the blade specifications is presented in Table 1.

Acoustic measurement

Acoustic measurements were conducted using a Bionic M-112 two-dimensional planar microphone array, which has a diameter of 1 m and consists of 112 micro-electro-mechanical systems (MEMS) microphones. The microphone distribution of the array is shown in Figure 4(a). The microphone array was placed on the ground, with its plane tilted at 55° to face the wind turbine rotor. The horizontal and vertical distances between the microphone array center and the rotor rotational center were 3.0 and 2.9 m, respectively. The microphone array center was 0.48 m below the bottom edge of the OJF nozzle, ensuring that all the microphones were out of the flow. With this configuration, the spatial resolution varies from about 2.5 m at 500 Hz to 0.25 m at 5000 Hz, covering the wind turbine rotor in the mid-to-high frequency range relevant for blade damage-induced acoustic features.

Table 1. A summary of blade specifications.

Parameter	Dimension
Rotor radius, *R*	1250 mm
Net length, *L*	1200 mm
Shell thickness of the pressure and suction sides	~2 mm
Shear web thickness	~4 mm
First shear web location	26.0% *C*
Second shear web location	42.5% *C*
Damage location (center)	50% *R* (mid-span)
Damage length	12.5 mm (10% *R*)

For each microphone channel, the sampling frequency was set to 48 kHz, with a 24-bit resolution. The microphone array was capable of measuring sound pressure levels ranging from under 33 to 120 dB. In the experiment, the acoustic data were recorded for 30 s for each case. The signal was separated into time chunks of 8192 samples with 50% data overlap for the Fourier transform. For each chunk, a Hanning weighting function was applied to reduce the energy leakage. The configuration provides a frequency resolution of 5.86 Hz. The cross-spectral matrix was averaged from the obtained auto-spectra of the Fourier transform. Conventional frequency domain beamforming (CFDB)[44,57] was performed to localize and visualize the acoustic sources on the blade rotating plane with a size of 2.0 × 2.0 m centered at the rotating center. A source power integration technique[45] was applied to the box with a size of 1.5 × 1.5 m to get the integrated noise spectrum, as shown in Figure 4(b).

Thermal measurement

To achieve sufficient sensitivity and low integration time for the thermal measurements, a Cedip Titanium infrared camera equipped with a 25 mm focal-length lens, providing an FOV of 21° × 17°, was employed in the rotating experiments. This camera offers a spatial resolution of 320 × 256 pixels and a thermal sensitivity noise equivalent temperature difference (NETD) of better than 18 mK. The minimum integration time of the detector is 3 μs, adjustable in 1 μs increments. In this experiment, the camera was calibrated and operated with an integration time of 50 μs, selected as a compromise between achieving a sufficient signal-to-noise ratio and minimizing motion blur caused by the blade movement.

Three 500 W halogen lamps were used to heat the blade and the surrounding air, as shown in Figure 1. The lamps were positioned slightly below the table, approximately 0.5 m from the blade tip, and tilted upward to ensure heating along the entire blade surface. The lamps were manually controlled simultaneously and remained on throughout each measurement to provide a sufficient and stable heat source. For the internal delamination case, the blade was fixed in a downward position and pre-heated for 300 s. As the lamps also heated the tower, the infrared camera was placed on the left side upwind of the turbine rotor to capture images of the blade as it passed horizontally, and to mitigate background effects from the tower during post-processing. The camera was placed 1.40 m from the blade rotation center and 1.75 m from the rotation plane to avoid disturbing the flow, and was horizontally rotated toward the blade with a yaw angle of 28°. The configuration provided an FOV of 0.74 × 0.59 m. A trigger signal from the wind turbine, combined with a DG535 trigger-delay generator, allowed thermal images to be recorded at a fixed position when the blade of interest passed through the FOV of the camera. For each measurement, 600 frames were recorded. Non-uniformity correction (NUC) was manually applied before each measurement.

Verification

To establish a reference for the rotating tests and to examine whether the aeroacoustic and thermal phenomena associated with blade damage were present, verification measurements were first conducted on the blades under non-rotating conditions prior to the rotating tests.

Non-rotating tests for acoustic measurements were conducted in the Anechoic vertical open-jet tunnel (A-tunnel) of TU Delft.[58] The experimental setup is shown in Figure 5(a). The wind tunnel has a 0.4 × 0.7 m rectangular test section at the outlet. It can operate at free-stream velocities up to 45 m/s, maintaining a turbulence intensity below 0.1% across the full velocity range. The uniformity of free-stream velocity in the test section is within 0.5% relative to the velocity at the nozzle center. The blade was mounted horizontally above the wind tunnel nozzle using two clamps at the two ends of the blade to ensure its stability. This configuration minimizes unwanted vibrations, which may introduce a change in the geometry of the blade, for example, the angle of the attack, under aerodynamic load during measurement. The trailing edge at mid-span was fixed at 500 mm from the nozzle, with the chord line at mid-span aligned with the nozzle centerline. During the measurements, the wind tunnel operated at a free-stream velocity of 30 m/s. The boundary layer was tripped using 0.4 mm thickness zigzag strips at 20% on both pressure and suction sides. Due to setup constraints, a different microphone array,

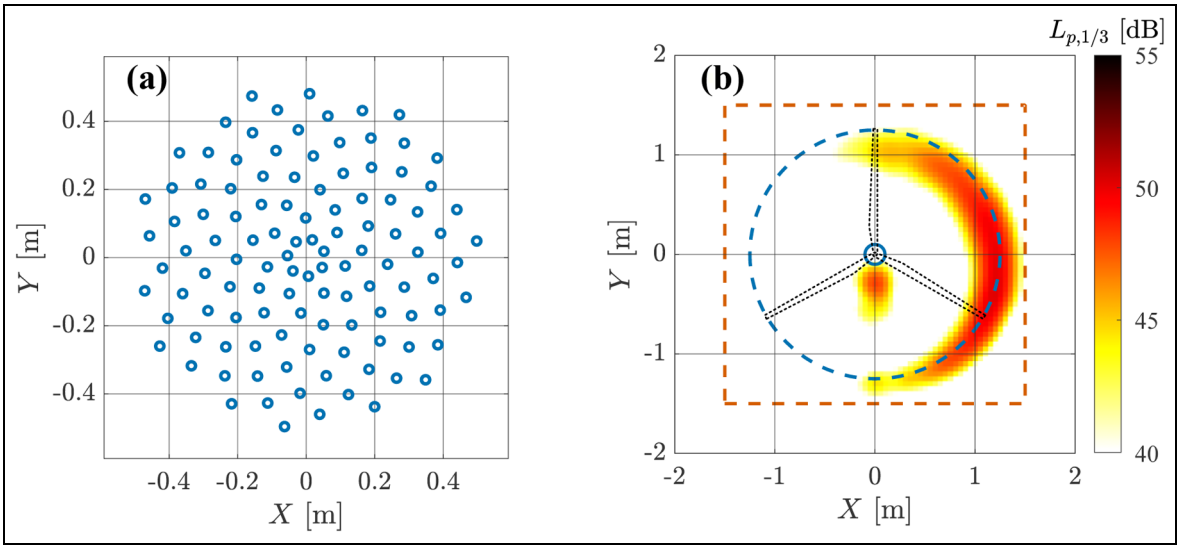

Figure 4. Acoustic measurement: (a) the distribution of the microphones of the array and (b) a representative beamforming map in one-third octave band with center frequency of $f_{1/3}$ = 3150 Hz; the solid circle is the rotor center; the dashed circle is the blade tip sweeping trajectory, and the orange dashed box indicates the source power integration region.

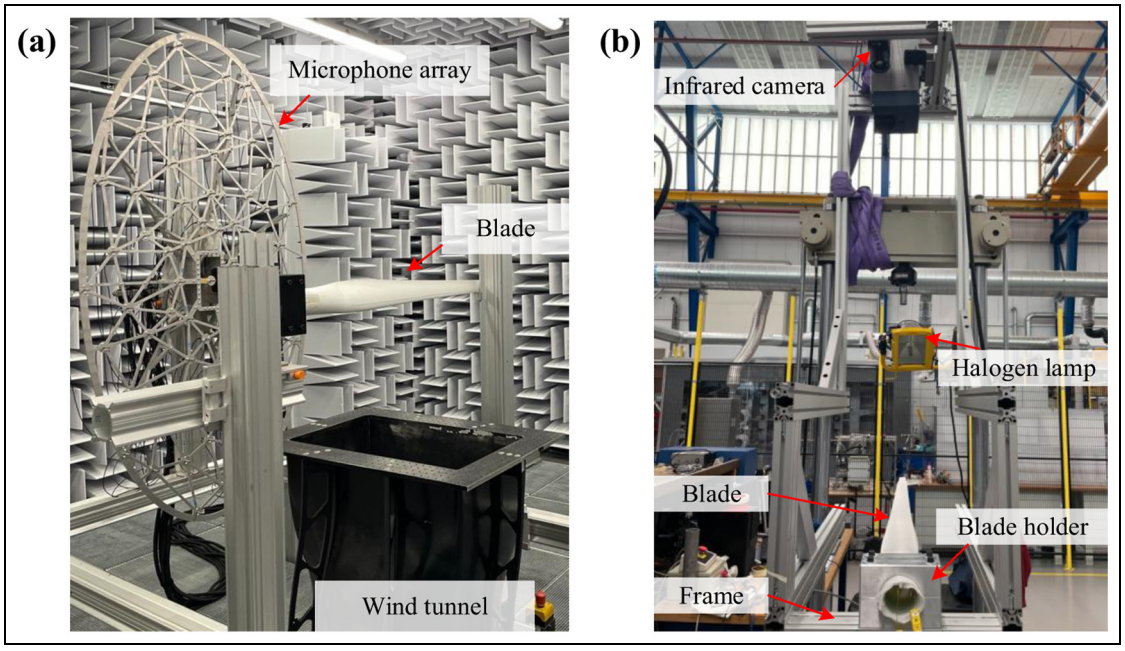

Figure 5. Experimental setup for non-rotating tests: (a) wind tunnel measurements and (b) static thermal measurements.

consisting of 64 *G.R.A.S. 40PH* free-field microphones, was employed in the verification tests. The microphone array provided similar performance to the Bionic M-112 and was used in the previous studies.[26,27,59] The sampling frequency of each microphone was 51.2 kHz. For each measurement, the acoustic data were recorded for 30 s and then separated into time blocks of 5120 samples with 50% overlap for the Fourier transform (Hanning weighted) and averaging, which provided a frequency resolution of 10 Hz. The same CFDB as described for the tests in the OJF was then performed on a square grid 1 × 1 m. The sound power was integrated within a 0.2 m (width) × 0.25 m (height) rectangular area centered at the blade trailing edge at mid-span. This configuration ensures the results obtained from the acoustic setup in the A-tunnel

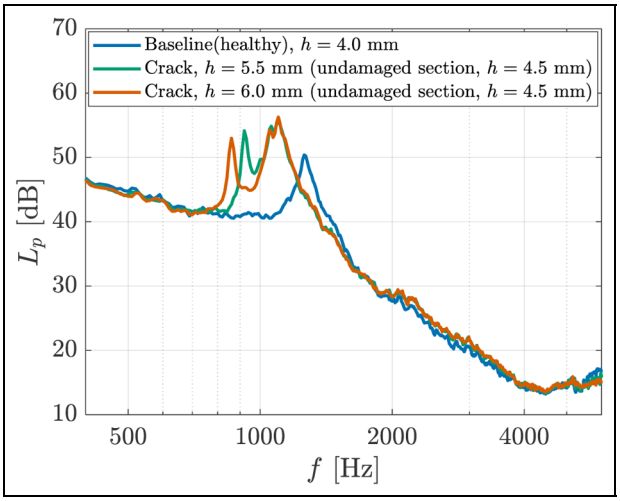

Figure 6. Noise spectra for the baseline and different cracked cases.

remain comparable with those measured in the OJF for the rotating tests.

The crack-induced increase in trailing edge thickness can alter the coherent vortex shedding process and, consequently, shift the associated tonal noise.[26,28] Figure 6 presents the noise spectra for the baseline and for different crack sizes under non-rotating conditions with a clean inflow. Table 2 summarizes the trailing edge thickness and the corresponding tonal frequency for each case, together with the trailing-edge-thickness-based Strouhal number, $St_{h,\,\mathrm{peak}} = \frac{f_{\mathrm{peak}} h}{U}$ (f_{peak}, h, and U are the tonal frequency, trailing edge thickness, and inflow velocity, respectively). The crack size was increased by introducing a small insert into the original cracked trailing edge.

For the baseline case, as shown in Figure 6, only a single spectral peak associated with blunt trailing edge noise is observed, since the trailing edge thickness is uniform along the span. This peak is located at $St_{h,\,\mathrm{peak}} = 0.168$, which agrees with the results reported in the study by Brooks et al.[53] When a crack appears at the trailing edge, two distinct peaks emerge in the noise spectrum. For the cracked blade, manufacturing differences lead to a slightly larger trailing edge thickness in the undamaged section compared to the healthy blade, causing the higher-frequency peak to shift toward a lower frequency relative to the baseline case. In addition, the presence of the crack further increases the trailing edge thickness at the damaged section, giving rise to an additional peak at a lower frequency. As the crack size increases, from a thickness of 5.5 to 6.0 mm, this low-frequency peak shifts further toward lower frequencies. A qualitative analysis shows that the corresponding trailing-edge-thickness-based Strouhal numbers, $St_{h,\,\mathrm{peak}}$, listed in Table 2, vary between 0.168 and 0.172. Moreover, as the crack size increases, the Strouhal number, $St_{h,\,\mathrm{peak}}$, tends to increase, which is consistent with the findings reported in the authors' previous work.[28]

Table 2. The crack size and frequency of the tone in the spectra and the corresponding $St_{h,\,\mathrm{peak}}$.

		Crack		
Case	Baseline	Undamaged section	Crack	Large crack
Trailing edge thickness, h (mm)	4.0	4.5	5.5	6.0
f_{peak} (Hz)	1260	1100	920	860
$St_{h,\,\mathrm{peak}}$	0.168	0.165	0.169	0.172

Static thermal measurements were performed in the DASML. A FLIR A655sc infrared thermal camera was employed in the verification tests. The camera was chosen for its high spatial resolution, and a short integration time was not required for the non-rotating blades. It is equipped with a 24.6 mm focal length lens corresponding to an FOV (in angle) of 25°×19°. The camera provided an image resolution of 640 × 480 pixels. The detector has a typical time constant of 8 ms. The thermal sensitivity (NETD) is better than 30 mK at 303.15 K and remains below 50 mK within the full measurement range. The blade was horizontally clamped on the aluminum frame at the blade root, as shown in Figure 5(b). The thermal camera was mounted on the top of the frame at a distance of about 1.5 m from the blade surface, which provided an FOV of 0.66 × 0.50 m. A 500 W halogen lamp was mounted approximately 0.3 m from the blade tip and 0.5 m above the blade at a tilt angle of about 45°, to heat the whole blade section within the FOV of the thermal camera while avoiding thermal reflections back to the camera. For each measurement, the blade was heated for approximately 300 s by manually controlling the lamp, after which the lamp was switched off. The thermal camera recorded the temperature variation during the blade heating phase and for an additional 300 s during the cooling phase at a recording rate of 1 Hz, resulting in approximately 600 frames for each case. NUC was performed before each measurement and disabled during recording, as the acquisition time was short.

To evaluate the capability of IRT in detecting structural damage, especially for the internal defects, the thermal responses for baseline and damaged blades were compared. Figure 7 shows the instantaneous thermal images when the blades were heated for

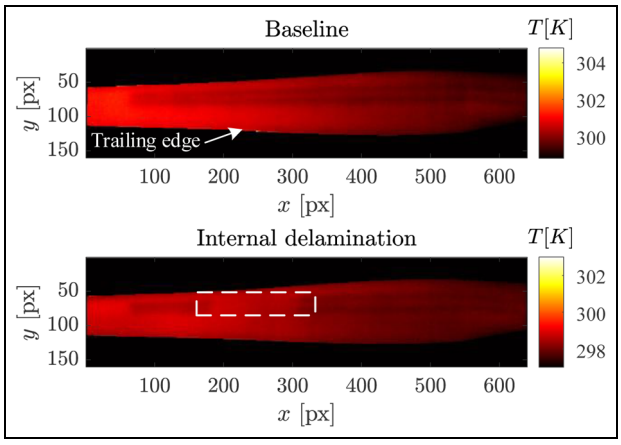

Figure 7. Instantaneous thermal image when the blade is heated for around 120 s for baseline and different damaged cases. The dashed box indicates the damaged location.

approximately 120 s for the baseline and internal delamination cases. The region with internal shear webs for both blades exhibits a slightly lower temperature compared to the surrounding area. In the case of internal delamination, the damaged region appears to exhibit less contrast with the surrounding area than the non-damaged location and at the same location as the baseline case. This behavior can be attributed to the disruption of heat conduction caused by the delamination, which introduces an additional thermal resistance. As a result, the heat flux is partially impeded, leading to localized temperature accumulation.

To further quantitatively examine the influence of the internal structure and delamination on the surface temperature distribution, Figure 8 presents the temperature profiles and their gradients for the baseline and internal delamination cases at two representative locations, $x = 250$ and $x = 450$. To mitigate the impact of numerical differentiation, a second-order regression with a window size of five points was applied to calculate the gradient from the temperature fields. In the delamination case, the profile at the location $x = 250$ passes directly through the damaged region. For the

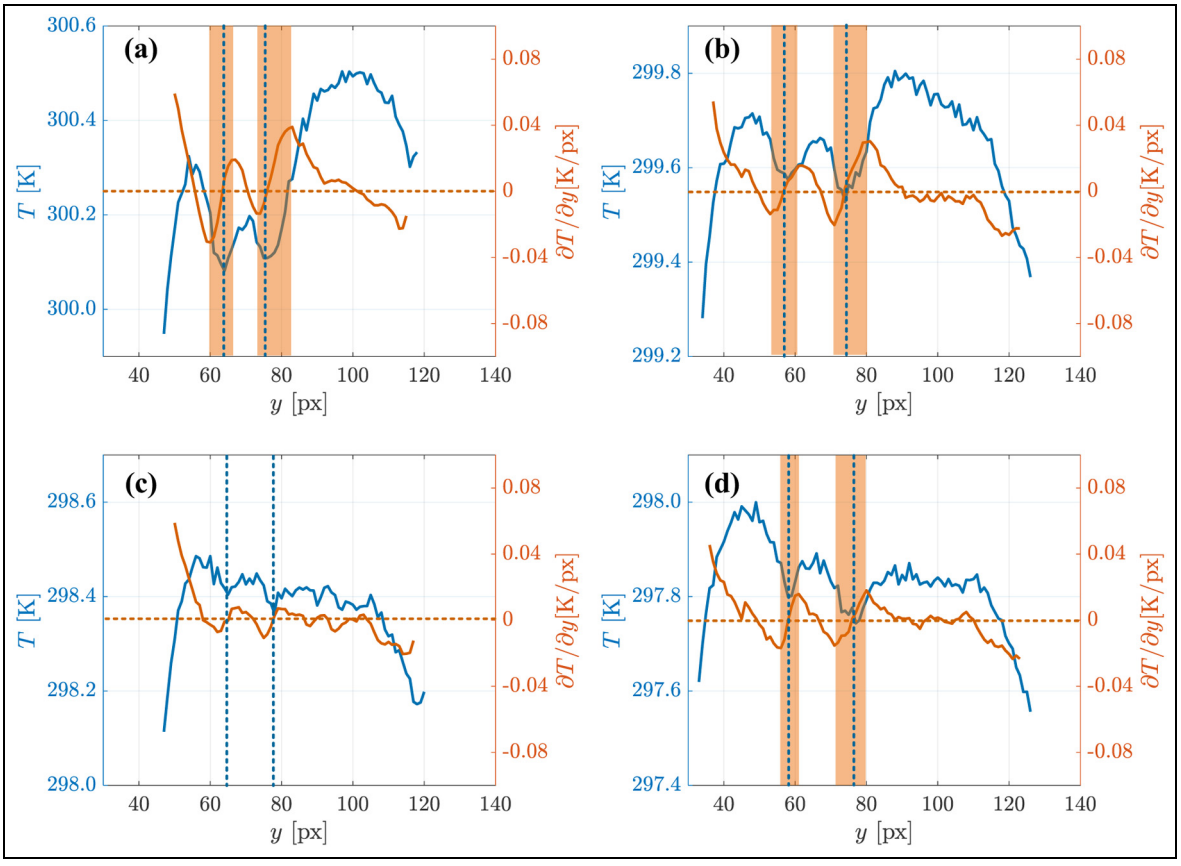

Figure 8. Temperature profiles and gradients at different locations for baseline and internal delamination cases: (a) baseline at $x = 250$, (b) baseline at $x = 450$, (c) internal delamination at $x = 250$ (damaged location), and (d) internal delamination at $x = 450$. The blue dashed lines indicate the potential shear web locations; the orange lines present the zero temperature gradient, and the orange areas are the estimated width of the shear web.

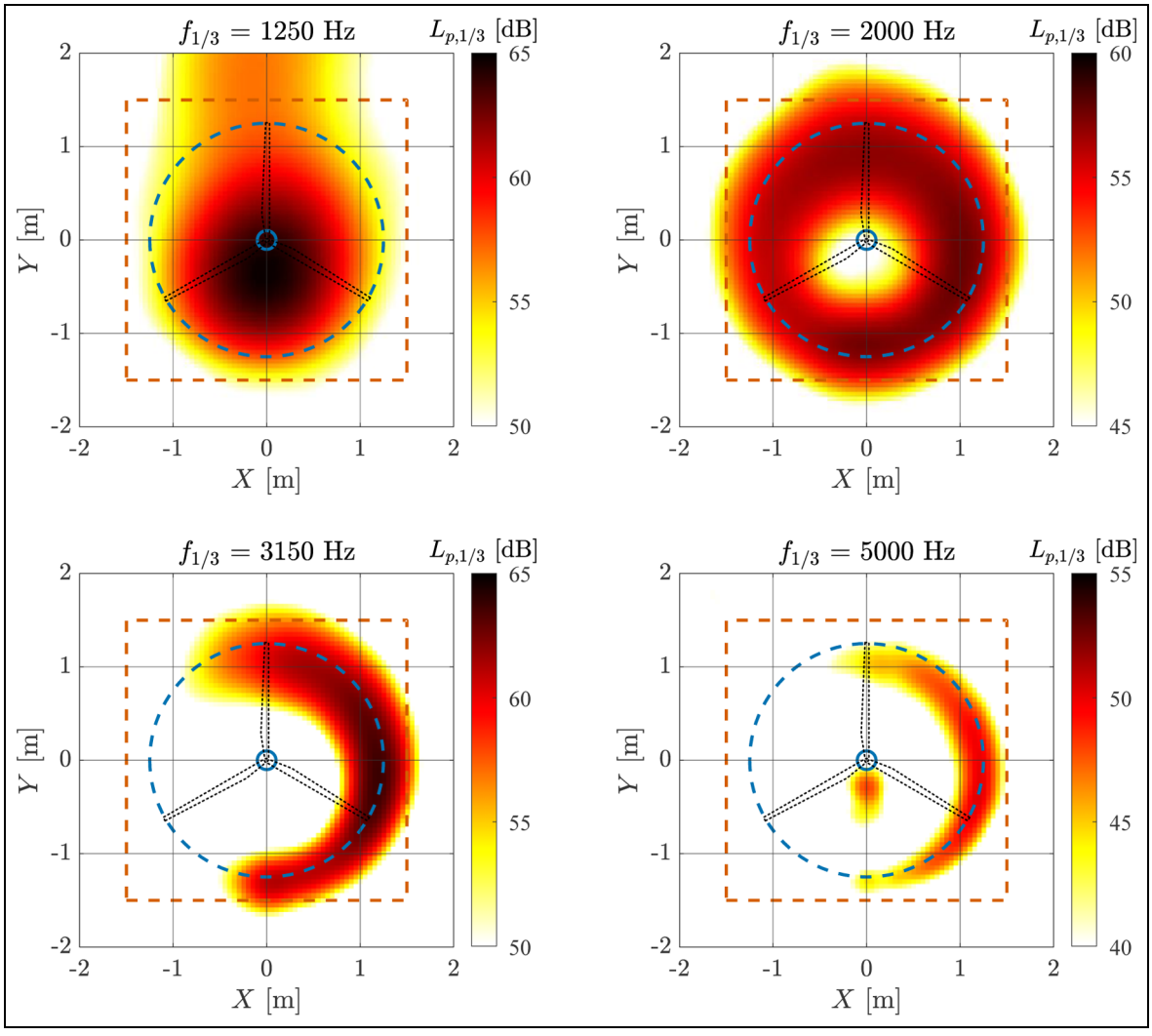

Figure 9. Beamforming maps at different representative one-third octave bands. The solid circle is the rotor center; the dashed circle is the blade tip sweeping trajectory, and the orange dashed box indicates the source power integration region.

undamaged sections of the blades, shown in Figure 8(a), (b), and (d), the surface temperature over the two internal shear webs is lower than that of the surrounding regions, with a maximum difference of about 0.5 K. These valleys in the profile mark the centerlines of the shear webs (the dashed blue lines in Figure 8). The associated temperature gradients emphasize the local variations in the temperature profiles: valleys in the gradient curves indicate transitions from warmer to cooler regions, whereas peaks represent transitions in the opposite direction. As illustrated in Figure 8, the area between a valley and a peak (highlighted in orange) represents the estimated width of the internal web. Zero crossings of the gradient curve correspond to local maxima and minima, which can potentially mark the centerlines of the internal shear webs, as indicated by the intersections with the orange dashed lines in Figure 8. In contrast, as shown in Figure 8(c), the temperature distribution of the damaged section differs from that of the undamaged regions. The delaminated region shows no distinguishable difference with the surrounding temperature, since the air void replaces the adhesive in the damaged section, and its thermal behavior is closer to that of the blade internal cavity.

Results and discussion

Acoustic detection

Noise sources and background noise. Beamforming was applied to process the acoustic data measured in the OJF experiments. Figure 9 shows the beamforming maps at several representative one-third octave bands (where $f_{1/3}$ is the center frequency of one-third octave

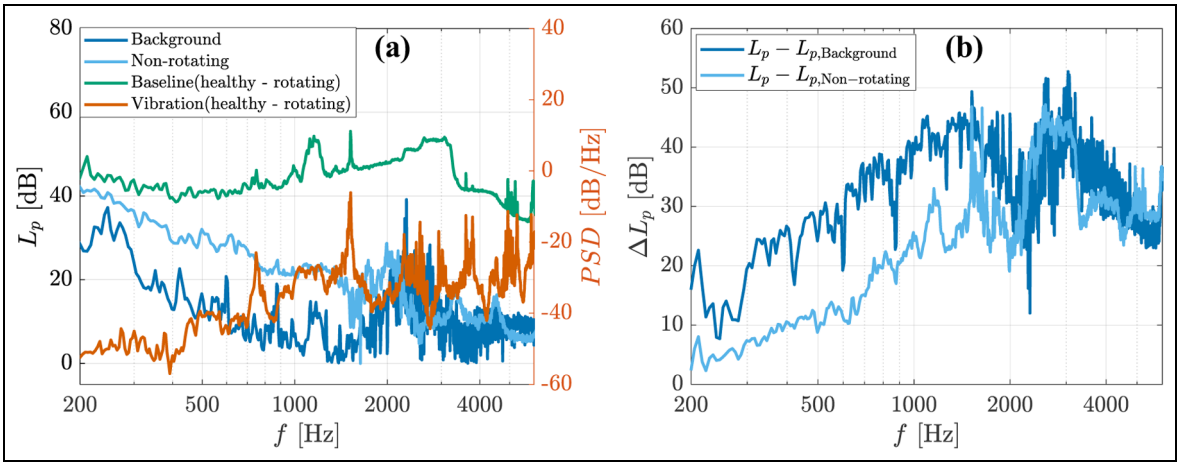

Figure 10. Background noise of the wind tunnel, and the relative noise levels and vibration of the wind turbine: (a) the noise levels of the wind tunnel and the non-rotating/rotating wind turbine; (b) the relative sound pressure level compared to the wind tunnel background noise and the non-rotating case.

band) for the baseline configuration (where all the blades are healthy) under an inflow velocity of 7 m/s and a rotational speed of 420 rpm. It should be noted that, due to the Rayleigh limit,[60] conventional beamforming based on the configuration of the microphone array in this study is not able to identify the noise sources at low frequencies. Since the source power integration is applied within the dashed box shown in Figure 9, the background noise from the wind tunnel can be mitigated. Figure 10(a) compares the spectra of the wind tunnel background noise with those of the wind turbine under non-rotating and rotating conditions. To better distinguish between aerodynamic and mechanical noise sources, the power spectral density of the vibration signal (fore–aft direction) from the accelerometer mounted on the main bearing housing is shown for comparison. The relative sound levels of the rotating wind turbine regarding the wind tunnel background noise and non-rotating condition are shown in Figure 10(b).

Within the frequency range of 300–2000 Hz, the wind tunnel background noise is approximately 20 dB lower than that of the rotating wind turbine. When the inflow is present (7 m/s), the noise level of the rotating wind turbine remains about 10 dB higher than that of the non-rotating case in the 500–2000 Hz range. These results indicate that, although the OJF wind tunnel was not originally designed as an anechoic facility, it nevertheless provides a sufficiently low background noise level to enable reliable acoustic measurements. Similar observations were reported in a previous preliminary investigation.[23]

The wind turbine noise in the 500–2000 Hz frequency range, which is relevant for damage detection, as shown in Figure 10, exhibits a broadband characteristic, indicating that trailing edge turbulence noise is dominant. In addition, three discrete tonal peaks are observed at center frequencies of 750, 1150, and 1520 Hz. These peaks also appear in the vibration signal, suggesting that they originate from the mechanical components of the wind turbine. The beamforming map at the one-third octave center frequency of $f_{1/3} = 1250$ Hz, shown in Figure 9, further indicates that this tonal component at 1150 Hz is primarily generated at the wind turbine center.

Trailing edge crack detection. A crack at the trailing edge can lead to an increase in the local effective thickness, as the crack opening introduces a geometric modification[3] that affects aerodynamic noise. In this work, the damage size was adjusted by adding different layers of tape to the damaged section, thus increasing the total thickness of the trailing edge. Experiments were conducted at a rotational speed of 420 rpm and a wind speed of 7 m/s. All the blades were tripped using 0.4 mm thickness zigzag strips on both the suction and pressure sides at 20% of the chord. Figure 11 shows the noise spectra for the baseline and the various cracked configurations. It should be noted that, since the experiments in the A-tunnel and OJF were performed in different seasons, the trailing edge thickness of the original crack slightly changed from 5.5 mm, as shown in Table 2, to 4.85 mm. As shown in Figure 11, the noise spectra of the baseline case and the 4.85 mm cracked case are very close below 1300 Hz, where the damage-induced features are not clear. A noticeable difference between the two configurations appears in

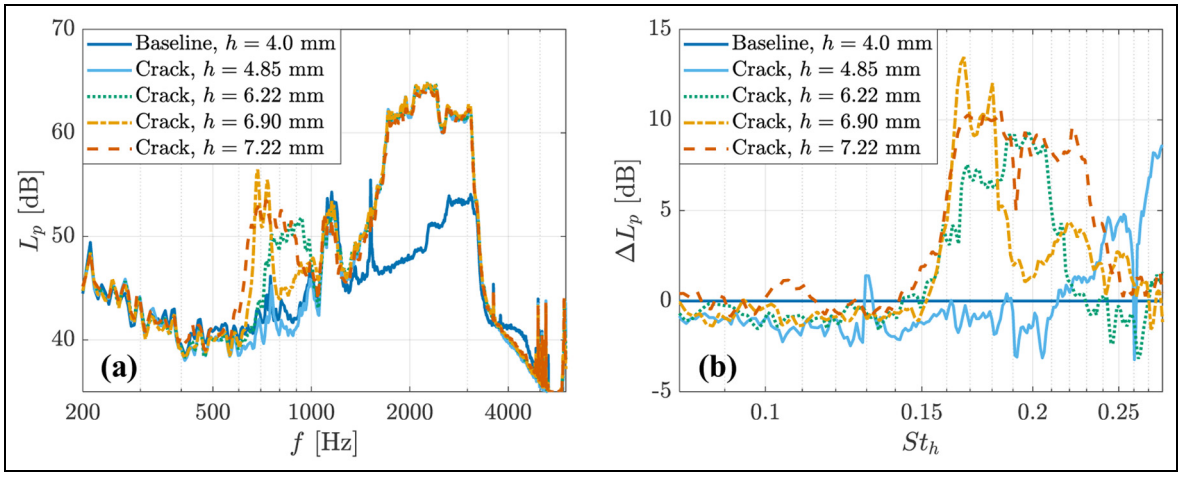

Figure 11. The sound pressure level and the relative sound pressure level for baseline and trailing edge crack of different crack sizes: (a) noise spectra and (b) relative spectra compared to the baseline case.

the 1700–3000 Hz range, where the noise spectrum of the cracked blade exhibits a higher-level broadband hump compared to the baseline. Figure 12 shows the beamforming maps for these two cases at a one-third octave frequency of $f_{1/3} = 2500$ Hz with the same dynamic range (60–75 dB). The cracked configuration exhibits a markedly higher sound pressure level near the blade tip, which may be attributed to a slight tip deformation after manufacturing, leading to a small twist that generates increased noise in this region. However, this change does not affect the detection of the trailing edge crack, as the crack-induced spectral variations are present at lower frequencies.

For a larger crack, the trailing edge thicknesses were set to $h = 6.22$, 6.90, and 7.22 mm. Strong tonal components appear in the corresponding noise spectra, as shown in Figure 11(a). As the crack size (trailing edge thickness) increases, the tonal components shift to lower frequencies, consistent with the expected effect of the blunter trailing edge. Figure 11(b) shows the relative sound pressure level compared to the baseline case, $\Delta L_p = L_p - L_{p,\text{Baseline}}$. The frequency is scaled by the trailing-edge-thickness-based Strouhal number, $St_h = fh/U$, where U is the resultant flow speed at the damaged section. The resultant flow speed, U, is obtained from BEMT, as shown in Table 3. The humps induced by damage are located in the range of St_h between 0.15 and 0.25, which agrees with the results reported in previous studies.[26,53]

To investigate how operating conditions, such as under different tip speed ratios, λ, corresponding to varying Reynolds numbers (based on chord length) and local angles of attack, affect damage detection, the wind turbine was tested at different rotational speeds while maintaining a constant inflow velocity of 7 m/s.

Table 3. The angular rotational speed, tip speed ratio, resultant flow speed, the local chord-based Reynolds number, and angle of attack at the damaged section.

Case no.	1	2	3	4
Rpm	180	300	420	540
λ	3.37	5.61	7.85	10.10
U (m/s)	13.69	20.79	28.27	35.91
Re_C	7.05×10^4	1.07×10^5	1.46×10^5	1.84×10^5
α (°)	25.34	13.13	7.07	3.96

The test matrix is summarized in Table 3. The resultant flow speed, U, and local angle of attack, α, at the damaged location were calculated using BEMT. Figure 12 presents the noise spectra and the relative spectra for the $h = 6.22$mm crack case with respect to the baseline configuration under the same operational conditions.

At a low rotational speed of 180 rpm, the high-frequency content in the noise spectrum is reduced, with pronounced high-level harmonics (characterized as laminar boundary layer instability noise,[61] due to low Reynolds number), while the low-frequency components remain similar to those at 420 rpm. The observed changes in the broadband distribution are attributed to the high local angle of attack, which promotes the formation of larger-scale vortices on the suction side.[62] When the rotational speed increases to 540 rpm, distinct low-frequency harmonics related to the blade passing frequency (f_B) appear in the spectrum (8–14 f_B observed), indicating the presence of loading noise.[63] For the low-speed cases (180 and 300 rpm, corresponding to low tip speed ratios), the damage-induced humps are absent in both the noise and relative spectra. This is attributed to the absence of coherent

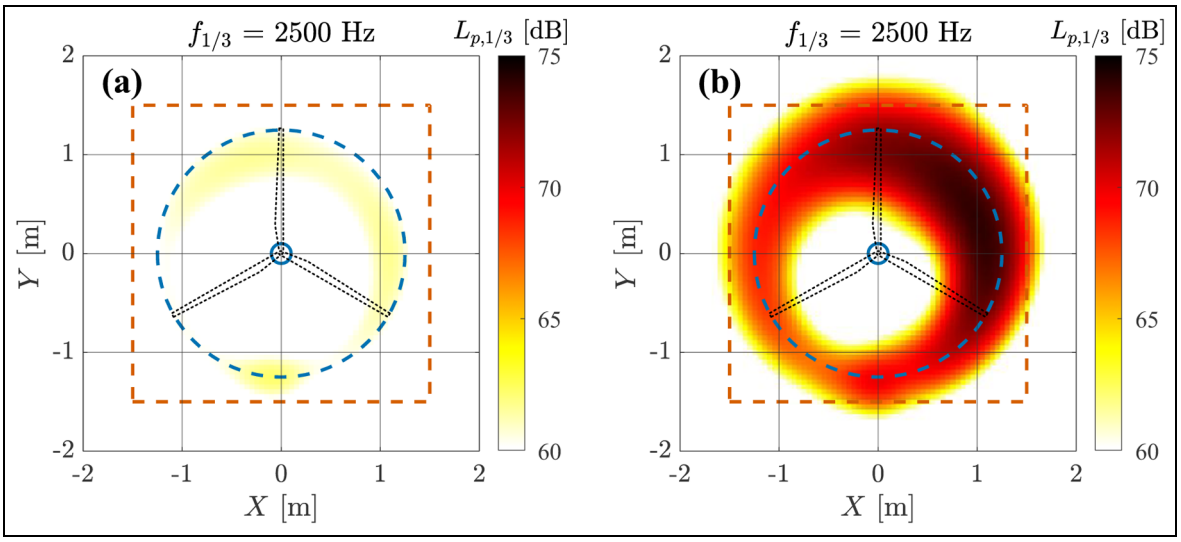

Figure 12. Beamforming maps at $f_{1/3} = 2500$ Hz for different configurations: (a) baseline and (b) crack ($h = 4.85$ mm); the dashed circle is the blade tip sweeping trajectory, and the orange dashed box indicates the source power integration region.

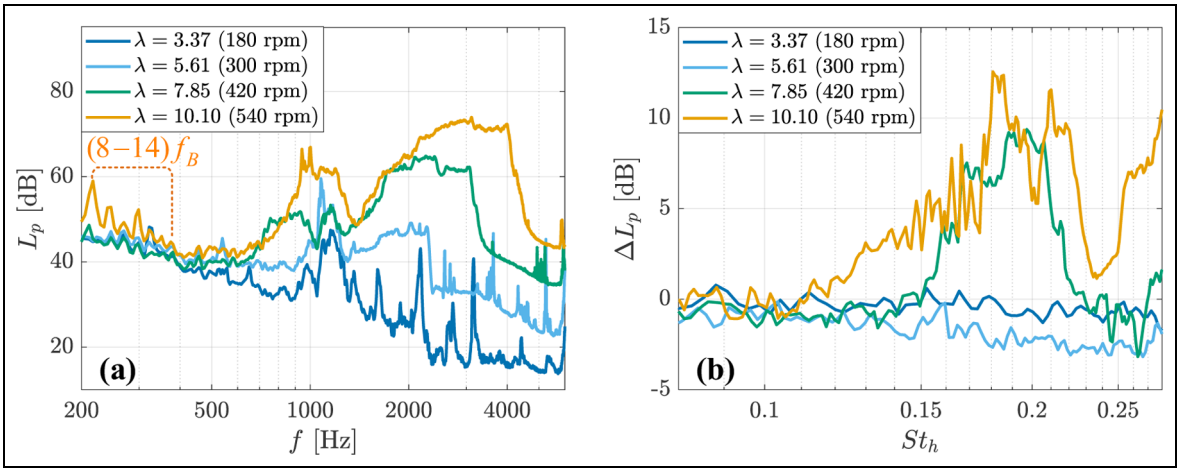

Figure 13. The sound pressure level and the relative sound pressure level for trailing edge crack configuration ($h = 6.22$ mm) at different tip speed ratios: (a) noise spectra and (b) relative spectra compared to the baseline case under the same operational condition.

vortex shedding due to the asymmetry of boundary layers on the suction and pressure sides at high angles of attack.[26,28] At a higher rotational speed of 540 rpm, the damage-induced spectral hump becomes more pronounced and shifts toward higher frequencies compared to the 420 rpm case, while peaking at a similar Strouhal number, St_h, as shown in Figure 13(b).

Thermal detection

Thermal features from the single image. Subsurface defects or damage potentially introduce air voids, resulting in a locally reduced effective thermal conductivity compared to the unaffected area. However, these subsurface or internal damage or defects may not significantly change the aerodynamic noise, making them difficult to identify using aeroacoustic features alone. Figure 14 shows the instantaneous thermal images for both baseline and delamination cases. In the experiment, the blades were pre-heated for around 300 s. For the baseline blade, a tripping zigzag strip was placed at 20% of the chord on both the suction and pressure sides, which appears as a clear line in the thermal image. The regions corresponding to the internal shear webs

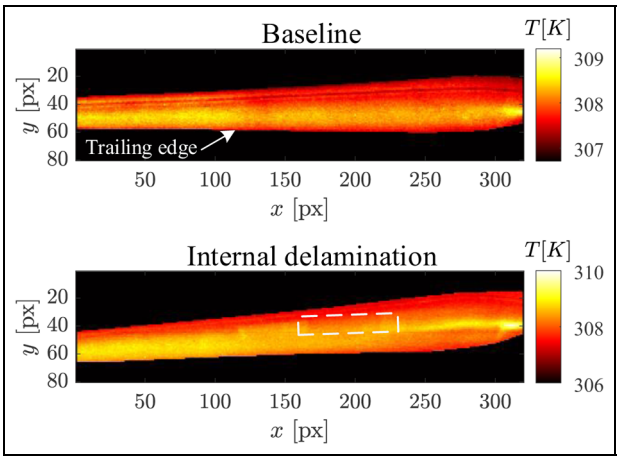

Figure 14. Thermal images for the baseline case and the case with internal delamination. The dashed box indicates the damaged location.

exhibit lower surface temperatures than the blade cavity regions. This observation is consistent with the non-rotating blade results, as the blade cavity restricts heat dissipation, leading to greater temperature accumulation at the surface. For the blade with internal delamination, the tripping strips were moved close to the leading edge to minimize their influence on visualizing the internal shear webs. The damaged location exhibits a clear thermal discontinuity due to the absence of adhesive, where a lower surface temperature is observed, highlighting the sensitivity of IRT to internal delamination. This behavior in the temperature field is inconsistent with the non-rotating case. This difference can be attributed to the stronger flow convection effects associated with blade rotation, which enhance heat dissipation. As a result, the temperature at the damaged location (the air void), which has a significantly lower volumetric heat capacity, decreases more rapidly than that in the intact regions.

PC thermography. To further enhance the visibility of temperature features associated with internal structures and defects, PCT is applied to the thermal image sequences. In this study, 500 thermal images were used for the PCT analysis. Figure 15 shows the first four PCs for the baseline and internal delamination cases. For the baseline case, the first three PCs clearly show the internal shear webs (at 26.0% and 42.5% of the chord length) together with the surface zigzag tripping strip (at 20% chord), while the fourth PC shows only the tripping strip. In contrast, for the internal delamination case, discontinuities in the internal shear web patterns are evident in PCs 2 and 3, indicating the presence of internal delamination.

The thermal images are reconstructed using only the PCs associated with internal features to ensure consistency with the analysis framework used for the non-rotating blades discussed in the third section. Figure 16 shows the reconstructed instantaneous thermal images for the baseline and internal delamination cases. For the baseline blade, the reconstruction is performed using PCs 1–3, whereas for the internal delamination case, only PCs 2 and 3 are used. After reconstruction, the thermal features associated with the internal structures become more pronounced than in the original images shown in Figure 14. The internal delamination is more clearly visualized, appearing as a higher-temperature discontinuity at the damaged location. This behavior is attributed to the reduced effective thermal conductivity at the delaminated section, which impedes heat transfer and leads to localized heat accumulation, as discussed previously.

Figure 17 shows the temperature profiles and gradients sampled from the reconstructed temperature fields for baseline and internal delamination cases at different representative pixel locations. The window size of the second-order regression was set to three points due to a lower resolution compared to the verification tests when calculating the gradient. For the baseline case along $x = 200$, the zigzag tripping strip close to the first shear web results in large temperature variations, which obscure the identification of the internal structural features. At the location of the second shear web, the temperature profile exhibits a distinct valley accompanied by a zero crossing in the temperature gradient, consistent with the results reported in the third section.

For the internal delamination case, at the healthy section near the shear web tips ($x = 150$), the temperature profiles and gradients exhibit the typical thermal features of the two internal shear webs: the temperature profiles show valleys of approximately -0.1 K with zero gradient at the minima, while the effective shear web width can be estimated from the region between a valley and a peak in the gradient curve. At the near-root section ($x = 250$), a similar thermal pattern is observed; however, the distinction between the two shear webs becomes less pronounced, as the two valleys tend to merge. This behavior is potentially due to the formation of a laminar separation bubble in the boundary layer under low Reynolds number conditions close to the blade root over the shear web locations. The associated external thermal effects can hide the thermal features of the internal structures.

At the internal delamination location ($x = 200$), the two shear webs remain identifiable but exhibit a reduced temperature contrast (approximately -0.06 K) compared to the same blade at the healthy locations ($x = 150$ and $x = 250$). The results demonstrate

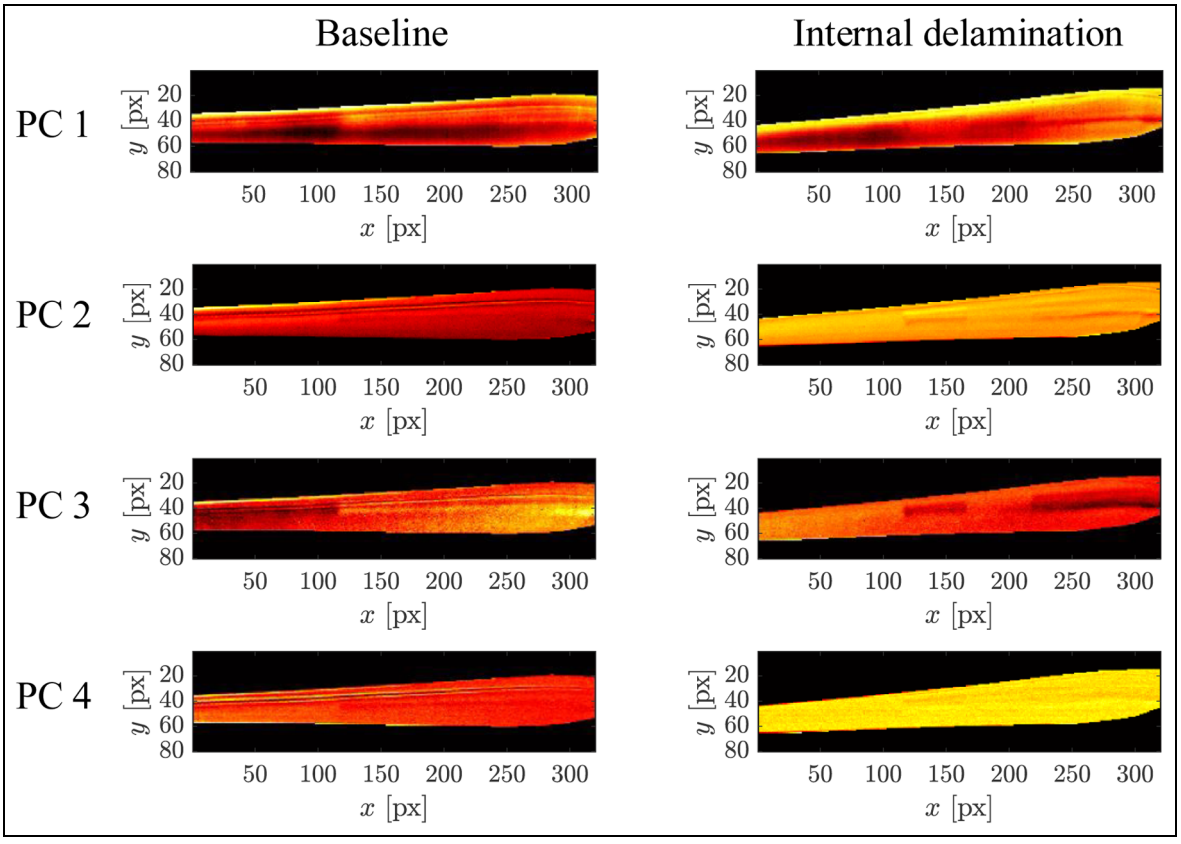

Figure 15. The first four PCs of PCT for the baseline case and the case with internal delamination. PC: principal component; PCT: principal component thermography.

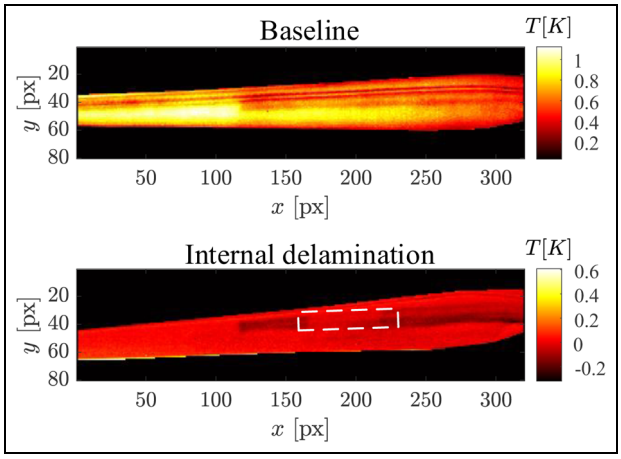

Figure 16. The reconstructed thermal images for the baseline case (using PCs 1–3) and the case with internal delamination (using PCs 2 and 3). PC: principal component.

that thermal measurements, particularly when combined with appropriate post-processing, can effectively visualize internal structural features and detect internal defects or damage.

Conclusions

This work experimentally investigated the feasibility of aeroacoustic and IRT techniques for damage detection in rotating wind turbine blades in the wind tunnel. Two types of subsurface and internal damage, including trailing edge crack and internal shear web delamination, were examined under controlled operating conditions to evaluate the sensitivity and complementarity of the two methods.

The aeroacoustic results demonstrate that subsurface edge damage, such as trailing edge cracks, induces distinct aeroacoustic modifications. The crack-induced tonal noise exhibits a clear dependence on trailing edge thickness, which shows a peak at a trailing-edge-thickness-based Strouhal number, St_h, between 0.15 and 0.25, and can be effectively identified using spectral analysis and beamforming techniques. However, the internal defects do not necessarily generate observable aerodynamic noise features, limiting the applicability of aeroacoustics for detecting such damage. In practical wind turbine applications, mechanical noise from the drivetrain can be isolated by using beamforming and applying advanced spectral analysis techniques

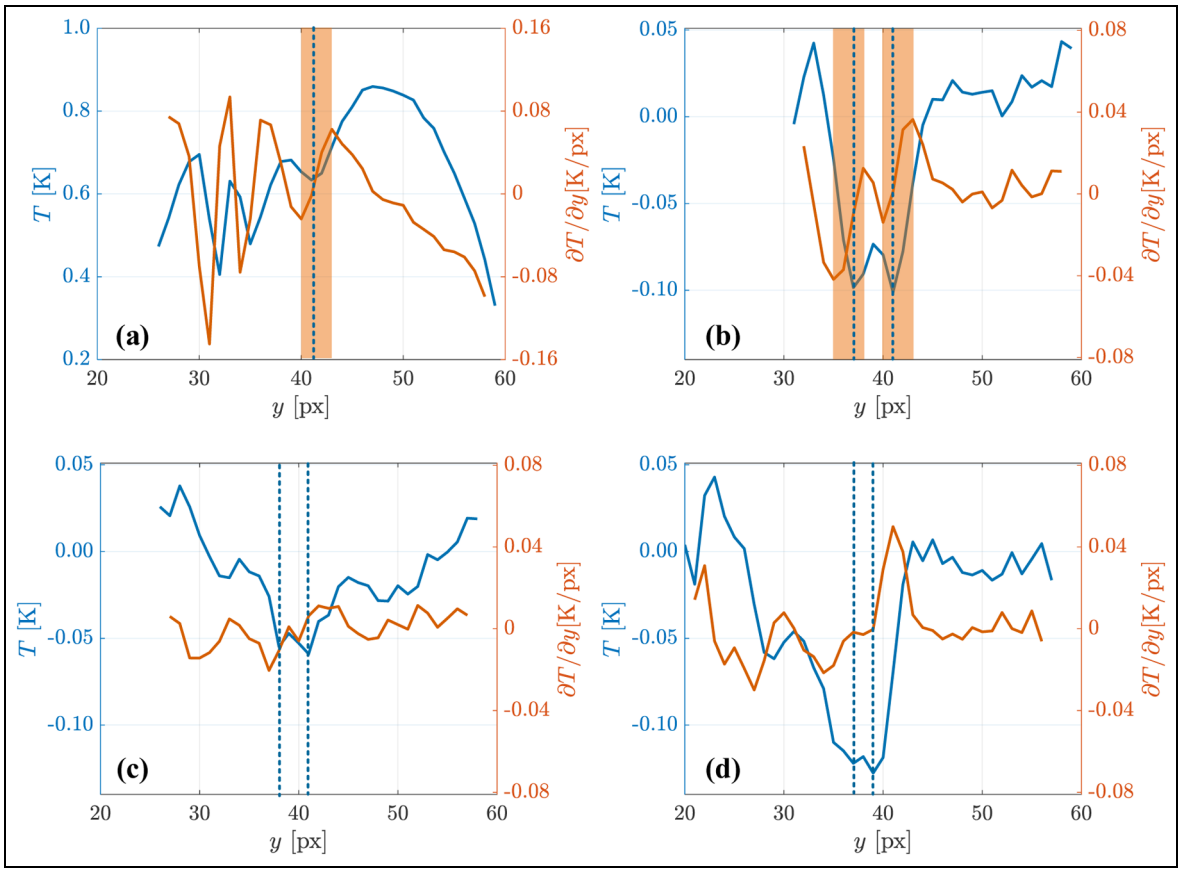

Figure 17. The temperature profiles and gradients of the reconstructed temperature fields for different cases at various representative pixel locations: (a) baseline at $x = 200$, (b) internal delamination at $x = 150$, (c) internal delamination at $x = 200$ (damaged location), and (d) internal delamination at $x = 250$. The blue dashed lines indicate the potential shear web locations, and the orange areas are the estimated width of the shear web.

based on its different spectral characteristics compared to aerodynamic noise sources.

IRT, on the other hand, shows strong sensitivity to internal structural features through their influence on heating and dissipation properties. Internal delamination introduces air voids with reduced effective thermal conductivity and volumetric heat capacity, leading to localized heat accumulation or dissipation and measurable surface temperature differences. The application of PCT can enhance the visibility of internal shear webs and delamination.

Combining aeroacoustics and IRT enables the detection of both subsurface damage at the blade edge and internal structural defects. This mitigates the individual limitations of each method, such as the insensitivity of aeroacoustics to internal damage and the spatial resolution and motion-induced constraints of IRT for the blade edge. The results suggest that a multi-technique framework has the potential to provide a more comprehensive and robust strategy for wind turbine blade damage detection.

Future work will focus on a deeper integration of acoustic and thermal imaging data, such as data-level or feature-level data fusion, and machine learning algorithms within a unified framework, to further enhance the effectiveness and reliability of the proposed measurement methods for blade damage detection, achieving comprehensive and automatic fault diagnosis.

In contrast to a wind tunnel, the inflow in a wind farm is typically unsteady and turbulent, which creates additional noise sources, for example, leading edge noise. Solar heating on the blade is generally stronger and more uniformly distributed than artificial heating, leading to a more pronounced thermal contrast between healthy and damaged regions. However, defects located at varying depths may be difficult to detect based on thermal variations observed on the blade surface. The proposed approach will be further validated in more complex operational scenarios using measurements on real-world megawatt-scale wind turbines.

Acknowledgment

The authors would like to thank Dr Roberto Merino Martinez for his help and suggestions on acoustic data processing.

ORCID iDs

Yanan Zhang https://orcid.org/0000-0001-9024-5789
Sumit K. Pal https://orcid.org/0000-0003-3762-8355
Roger M. Groves https://orcid.org/0000-0001-9169-9256

Funding

The authors disclosed receipt of the following financial support for the research, authorship, and/or publication of this article: This work was supported by the Dutch Research Council (NWO) under the project *Holi-DOCTOR:* Holistic Framework for Diagnostics and Monitoring of Wind turbine Blades (grant no. KICH1.ED02.20.004).

Declaration of conflicting interests

The authors declared no potential conflicts of interest with respect to the research, authorship, and/or publication of this article.

Data availability statement

Data will be made available on request.

References

1. Watson S, Moro A, Reis V, et al. Future emerging technologies in the wind power sector: a European perspective. *Renew Sustain Energy Rev* 2019; 113: 109270. https://doi.org/10.1016/j.rser.2019.109270
2. Bilgili M and Alphan H. Global growth in offshore wind turbine technology. *Clean Technol Environ Policy* 2022; 24: 2215–2227. https://doi.org/10.1007/s10098-022-02314-0
3. Branner K and Ghadirian A. *Database about blade faults*, http://orbit.dtu.dk/files/118222161/Database_about_blade_faults.pdf (2014, accessed 5 February 2026).
4. Han W, Kim J and Kim B. Effects of contamination and erosion at the leading edge of blade tip airfoils on the annual energy production of wind turbines. *Renew Energy* 2018; 115: 817–823. https://doi.org/10.1016/j.renene.2017.09.002
5. Zhang S, Dam-Johansen K, Bernad PL, et al. Rain erosion of wind turbine blade coatings using discrete water jets: effects of water cushioning, substrate geometry, impact distance, and coating properties. *Wear* 2015; 328–329: 140–148. https://doi.org/10.1016/j.wear. 2015.01.079
6. Haselbach PU and Branner K. Initiation of trailing edge failure in full-scale wind turbine blade test. *Eng Fract Mech* 2016; 162: 136–154. https://doi.org/10.1016/j.engfracmech.2016.04.041
7. Li X li, Sun J, Tao N, et al. An effective method to inspect adhesive quality of wind turbine blades using transmission thermography. *J Nondestruct Eval* 2018; 37: 1–11. https://doi.org/10.1007/s10921-018-0473-5
8. Taylor SG, Park G, Farinholt KM, et al. Fatigue crack detection performance comparison in a composite wind turbine rotor blade. *Struct Heal Monit* 2013; 12: 252–262. https://doi.org/10.1177/1475921712471414
9. Yang C, Liu X, Zhou H, et al. Towards accurate image stitching for drone-based wind turbine blade inspection. *Renew Energy* 2023; 203: 267–279. https://doi.org/10.1016/j.renene.2022.12.063
10. Yang W, Peng Z, Wei K, et al. Structural health monitoring of composite wind turbine blades: challenges, issues and potential solutions. *IET Renew Power Gener* 2017; 11: 411–416. https://doi.org/10.1049/iet-rpg.2016.0087
11. Dao C, Kazemtabrizi B and Crabtree C. Wind turbine reliability data review and impacts on levelised cost of energy. *Wind Energy* 2019; 22: 1848–1871. https://doi.org/10.1002/we.2404
12. Du Y, Zhou S, Jing X, et al. Damage detection techniques for wind turbine blades: a review. *Mech Syst Signal Process* 2020; 141: 106445. https://doi.org/10.1016/j.ymssp.2019.106445
13. Zhang Y, Avallone F and Watson S. An aeroacoustics-based approach for wind turbine blade damage detection. *J Phys Conf Ser* 2022; 2265: 022088. https://doi.org/10.1088/1742-6596/2265/2/022088
14. Zhang XY, Zhou B, Li H, et al. Depth detection of spar cap defects in large-scale wind turbine blades based on a 3D heat conduction model using step heating infrared thermography. *Meas Sci Technol*; 33. Epub ahead of print 2022. https://doi.org/10.1088/1361-6501/ac41a8
15. Yang S and Allen MS. Output-only modal analysis using continuous-scan laser doppler vibrometry and application to a 20 kW wind turbine. *Mech Syst Signal Process* 2012; 31: 228–245. https://doi.org/10.1016/j.ymssp.2012.04.012
16. Yang B and Sun D. Testing, inspecting and monitoring technologies for wind turbine blades: a survey. *Renew Sustain Energy Rev* 2013; 22: 515–526. https://doi.org/10.1016/j.rser.2012.12.056
17. Tcherniak D and Mølgaard LL. Active vibration-based structural health monitoring system for wind turbine blade: demonstration on an operating Vestas V27 wind turbine. *Struct Heal Monit* 2017; 16: 536–550. https://doi.org/10.1177/1475921717722725
18. Marques R, Unel M, Yildiz M, et al. Remaining useful life prediction of laminated composite materials using thermoelastic stress analysis. *Compos Struct* 2019; 210: 381–390. https://doi.org/10.1016/j.compstruct.2018.10.047
19. Lighthill MJ. On sound generated aerodynamically. I. general theory. *Proc R Soc London A, Math Phys Sci* 1952; 211: 564–587. https://doi.org/10.1098/rspa.1952.0060
20. Ffowcs Williams JE and Hawkings DL. Sound generation by turbulence and surfaces in arbitrary motion. *Philos Trans R Soc London Ser A, Math Phys Sci* 1969; 264: 321–342. https://doi.org/10.1098/rsta.1969.0031

21. Rubio Carpio A, Merino Martínez R, Avallone F, et al. Experimental characterization of the turbulent boundary layer over a porous trailing edge for noise abatement. *J Sound Vib* 2019; 443: 537–558. https://doi.org/10.1016/j.jsv.2018.12.010
22. Teruna C, Avallone F, Casalino D, et al. Numerical investigation of leading edge noise reduction on a rod-airfoil configuration using porous materials and serrations. *J Sound Vib* 2021; 494: 1–25. https://doi.org/10.1016/j.jsv.2020.115880
23. Zhang Y. *Wind turbine blade damage detection using aerodynamic noise*. Delft University of Technology, 2024.
24. Chen B, Yu S, Yu Y, et al. Acoustical damage detection of wind turbine blade using the improved incremental support vector data description. *Renew Energy* 2020; 156: 548–557. https://doi.org/10.1016/j.renene.2020.04.096
25. Chen B, Zhang M, Lin Z, et al. Acoustic-based whistle detection of drain hole for wind turbine blade. *ISA Trans* 2022; 131: 736–747. https://doi.org/10.1016/j.isatra.2022.05.010
26. Zhang Y, Avallone F and Watson S. Wind turbine blade trailing edge crack detection based on airfoil aerodynamic noise: an experimental study. *Appl Acoust* 2022; 191: 108668. https://doi.org/10.1016/j.apacoust.2022.108668
27. Zhang Y, Avallone F and Watson S. Leading edge erosion detection for a wind turbine blade using far-field aerodynamic noise. *Appl Acoust* 2023; 207: 109365. https://doi.org/10.1016/j.apacoust.2023.109365
28. Zhang Y, Watson S, Ragni D, et al. On the impact of turbulent inflow and crack-induced blunt trailing edge on the flow field and far-field noise of an airfoil. *Phys Fluids* 2025; 37: 105145. https://doi.org/10.1063/5.0299883
29. Tao N, Anisimov AG and Groves RM. Shearography non-destructive testing of thick GFRP laminates: numerical and experimental study on defect detection with thermal loading. *Compos Struct* 2022; 282: 115008. https://doi.org/10.1016/j.compstruct.2021.115008
30. Yang R, He Y, Mandelis A, et al. Induction infrared thermography and thermal-wave-radar analysis for imaging inspection and diagnosis of blade composites. *IEEE Trans Ind Informatics* 2018; 14: 5637–5647. https://doi.org/10.1109/TII.2018.2834462
31. Huang Y, Chen CL and Chiang CH. Analyzing a series of thermal infrared images to identify defects using a hybrid approach that combines robust principal component analysis and image segmentation. *NDT & E Int* 2023; 137: 102818. https://doi.org/10.1016/j.ndteint.2023.102818
32. Dollinger C, Sorg M, Balaresque N, et al. Measurement uncertainty of IR thermographic flow visualization measurements for transition detection on wind turbines in operation. *Exp Therm Fluid Sci* 2018; 97: 279–289. https://doi.org/10.1016/j.expthermflusci.2018.04.025
33. Li Y, Yang Z wei, Zhu J tang, et al. Investigation on the damage evolution in the impacted composite material based on active infrared thermography. *NDT & E Int* 2016; 83: 114–122. https://doi.org/10.1016/j.ndteint.2016.06.008
34. Manohar A, Tippmann J and Lanza di Scalea F. Localization of defects in wind turbine blades and defect depth estimation using infrared thermography. *Sensors Smart Struct Technol Civil Mech Aerosp Syst 2012* 2012; 8345: 83451O. https://doi.org/10.1117/12.915256
35. Liu K, Yu Q, Liu Y, et al. Convolutional graph thermography for subsurface defect detection in polymer composites. *IEEE Trans Instrum Meas* 2022; 71: 1–11. https://doi.org/10.1109/TIM.2022.3205906
36. Jaeger BE, Schmid S, Grosse CU, et al. Infrared thermal imaging-based turbine blade crack classification using deep learning. *J Nondestruct Eval* 2022; 41: 1–15. https://doi.org/10.1007/s10921-022-00907-9
37. Chaudhuri S, Stamm M and Krankenhagen R. Weather-dependent passive thermography and thermal simulation of in-service wind turbine blades. *J Phys Conf Ser* 2023; 2507: 1–12. https://doi.org/10.1088/1742-6596/2507/1/ 012025
38. Doroshtnasir M, Tamara W, Rainer K, et al. On-site inspection of potential defects in wind turbine rotor blades with thermography. *Wind Energy* 2016; 19: 1407–1422. https://doi.org/10.1002/we.1927
39. Zhou G, Fu Y, Zhang Z, et al. Edge detection and depth evaluation of CFRP internal delamination defects based on differential image frequency domain preprocessing. *J Instrum* 2025; 20: P01027. https://doi.org/10.1088/1748-0221/20/01/P01027
40. Varghese N, Mahesh MM and Rajagopalan AN. Fast motion-deblurring of IR images. *IEEE Signal Process Lett* 2022; 29: 459–463. https://doi.org/10.1109/LSP.2022.3140685
41. Oswald-Tranta B. Temperature reconstruction of infrared images with motion deblurring. *J Sensors Sens Syst* 2018; 7: 13–20. https://doi.org/10.5194/jsss-7-13-2018
42. Oswald-Tranta B, Sorger M and O'Leary P. Motion deblurring of infrared images from a microbolometer camera. *Infrared Phys Technol* 2010; 53: 274–279. https://doi.org/10.1016/j.infrared.2010.04.003
43. Traphan D, Herraéz I, Meinlschmidt P, et al. Remote surface damage detection on rotor blades of operating wind turbines by means of infrared thermography. *Wind Energy Sci* 2018; 3: 639–650. https://doi.org/10.5194/wes-3-639-2018
44. Sijtsma P. Phased array beamforming applied to wind tunnel and fly-over tests. *SAE Tech Pap* 2010; 2010: 17–19. https://doi.org/10.4271/2010-36-0514
45. Merino-Martínez R, Sijtsma P, Carpio AR, et al. Integration methods for distributed sound sources. *Int J Aeroacoustics* 2019; 18: 444–469. https://doi.org/10.1177/1475472X19852945
46. Rajic N. Principal component thermography for flaw contrast enhancement and flaw depth characterisation in composite structures. *Compos Struct* 2002; 58: 521–528. https://doi.org/10.1016/S0263-8223(02)00161-7
47. Lignarolo LEM, Ragni D, Krishnaswami C, et al. Experimental analysis of the wake of a horizontal-axis wind-turbine model. *Renew Energy* 2014; 70: 31–46. https://doi.org/10.1016/j.renene.2014.01.020
48. Bertagnolio F. A wind turbine noise code benchmark–round 1. In: *8th International conference on wind turbine*

noise, Lisbon, 12–14 June 2019, pp. 1–12. Institute of Noise Control Engineering (INCE) Europe.
49. Bertagnolio F, Fischer A, Seel F, et al. Wind turbine noise code benchmark: a comparison and verification exercise. In: *10th International conference on wind turbine noise*, Dublin, Ireland, 21–23 June 2023, pp. 1–21. National Renewable Energy Laboratory (NREL).
50. van der Velden WCP and Casalino D. Towards digital noise certification of serrated wind turbines. In: *25th AIAA/CEAS aeroacoustics conference*, American Institute of Aeronautics and Astronautics, https://arc.aiaa.org/doi/10.2514/6.2019-2646 (2019, accessed 5 February 2026).
51. Timmer WA and Van Rooij RPJOM. Summary of the Delft University wind turbine dedicated airfoils. *J Sol Energy Eng Trans ASME* 2003; 125: 488–496. https://doi.org/10.1115/1.1626129
52. Wang S, Zhou Y, Alam MM, et al. Turbulent intensity and Reynolds number effects on an airfoil at low Reynolds numbers. *Phys Fluids* 2014; 26: 115107. http://doi.org/10.1063/1.4901969
53. Brooks TF, Pope DS and Marcolini MA. *Airfoil self-noise and prediction*. National Aeronautics and Space Administration, 1989.
54. Rudd CD, Long AC, Kendall KN, et al. *Liquid moulding technologies: resin transfer moulding, structural reaction injection moulding and related processing techniques*. Woodhead Publishing, 1997.
55. Landis GA, Krasowski MJ and Colozza AJ. *Passive cooling for mercury surface lander electronics*. Cleveland, 2024.
56. Song Z, Zhang W, Shi Y, et al. Optical properties across the solar spectrum and indoor thermal performance of cool white coatings for building energy efficiency. *Energy Build* 2013; 63: 49–58.
57. Oerlemans S. *Detection of aeroacoustic sound sources on aircraft and wind turbines*. PhD Thesis—Research UT, graduation UT, University of Twente, 2009, pp. 1–173.
58. Merino-Martínez R, Rubio Carpio A, Lima Pereira LT, et al. Aeroacoustic design and characterization of the 3D-printed, open-jet, anechoic wind tunnel of Delft University of Technology. *Appl Acoust* 2020; 170: 107504. https://doi.org/10.1016/j.apacoust.2020.107504
59. Luesutthiviboon S, Pereira LTL, Ragni D, et al. Aeroacoustic benchmarking of trailing-edge noise from NACA 633–018 airfoil with trailing-edge serrations. *AIAA J* 2023; 61: 329–354. https://doi.org/10.2514/1.J061630
60. Rayleigh. XXXI. Investigations in optics, with special reference to the spectroscope. *Lond Edinb Dublin Philos Mag J Sci* 1879; 8: 261–274. https://doi.org/10.1080/14786447908639684
61. Kingan MJ and Pearse JR. Laminar boundary layer instability noise produced by an aerofoil. *J Sound Vib* 2009; 322: 808–828. https://doi.org/10.1016/j.jsv.2008.11.043
62. Hutcheson FV and Brooks TF. *Effects of angle of attack and velocity on trailing edge noise*. AIAA-Paper 2004-1031, January 2004.
63. Kotwicz Herniczek MT, Feszty D, Meslioui SA, et al. Evaluation of acoustic frequency methods for the prediction of propeller noise. *AIAA J* 2019; 57: 2465–2478. https://doi.org/10.2514/1.J056658